

## Particle-size distribution and microstructures within simulated fault gouge

CHRIS MARONE\* and C. H. SCHOLZ

Lamont-Doherty Geological Observatory and Department of Geological Sciences, Columbia University,  
Palisades, NY 10964, U.S.A.

(Received 15 October 1988; accepted in revised form 31 March 1989)

**Abstract**—This paper presents an investigation of comminution mechanisms and microstructure development within simulated fault gouge. We sheared 4.0 mm thick layers of quartz sand between rough steel surfaces using a triaxial apparatus. The layers were sheared at constant effective normal stress of 100 MPa, under saturated drained conditions, and at 45° to the axis of cylindrical steel samples. Porosity changes were measured throughout shear and microstructural observations were carried out on the deformed layers. Two types of load paths were investigated for shear strains ( $\gamma$ ) between 0 and 3.3; either the shear stress was repeatedly cycled from zero to failure or the sample was sheared in a single-load cycle. Multiple-cycle experiments exhibit significantly more compaction than single-cycle experiments deformed to similar strains. Gouge layers from both sets of experiments contain oblique zones of localized shear (Riedel shears bands) after  $\gamma = 1.3$ –1.5. Gouge particles obey a fractal size distribution for the range 12.5–800  $\mu\text{m}$ ; i.e. particle density vs size follows a power law,  $N(n)/A = bn^{-D}$ , where  $N(n)$  is the number of particles in a size range,  $A$  is the area examined,  $n$  is the mean of the size range,  $b$  is a constant and  $D$  is the fractal dimension.  $D$  for particles within the bulk material increases with shear strain for  $\gamma <$  about 1.5 after which it remains  $2.6 \pm 0.15$ . This value of  $D$  agrees with that found for natural fault gouge and with that predicted by a comminution model in which fracture probability depends on the relative size of nearest-neighbor particles. Analyses of particles within shear bands indicate continued size reduction after  $\gamma = 1.5$ . These particles do not obey a fractal size distribution for the range 6.25–100  $\mu\text{m}$  due to a lack of particles larger than 25–50  $\mu\text{m}$ . The rate of comminution within the bulk layer decreases at about  $\gamma = 1.5$ , which coincides with the onset of shear localization. Our data indicate that comminution is driven by relative movement between particles and that gouge layers attain a steady state particle-size distribution at  $\gamma = 1.5$ . The porosity–strain data and microstructural observations show a correlation between the onset of shear localization and the rate of dilatancy with shear strain.

### INTRODUCTION

FAULT gouge is the accumulated wear product of slip between fault surfaces. Understanding the role of gouge in faulting and friction is an important part of the overall problem of fault mechanics. In this regard, laboratory studies have shown that rock friction is affected by the presence of gouge (e.g. Byerlee 1967, Scholz *et al.* 1972), gouge thickness (e.g. Byerlee & Summers 1976), mineralogy (e.g. Shimamoto & Logan 1981) and particle size (e.g. Dieterich 1981, Biegel *et al.* 1989). However, there has been little success in relating these dependencies to mechanical processes within gouge zones, despite the important role gouge may play in controlling the stability of natural faults (e.g. Marone & Scholz 1988). Furthermore, while laboratory studies indicate that shear-localization within simulated gouge is associated with a transition in the stability of frictional slip (e.g. Engelder *et al.* 1975, Byerlee *et al.* 1978, Chester 1988, Moore *et al.* 1988), the physical mechanisms responsible for shear localization and the subsequent transition in stability remain poorly understood. Important insights for understanding these phenomena are provided by studies of the initiation (Vardoulakis 1980) and development (Mandl *et al.* 1977, Muhlhaus & Vardoulakis 1987) of shear bands within granular materials and field studies

of cataclasis (Engelder 1974, Blenkinsop & Rutter 1986, Chester & Logan 1987).

The purpose of this paper is to describe comminution mechanisms and fabric development within simulated gouge. We document changes in particle-size distribution, shear strength and porosity with progressive shear strain, and we relate shear localization to changes in particle-size distribution and mechanical behavior. The data presented here may help to infer the mechanical properties and comminution mechanisms of natural faults from studies of natural fault gouge.

Textural studies of fault gouge have examined the relationships between shear strain, confining pressure (depth) and particle-size distribution (Engelder 1974, Anderson *et al.* 1980, 1983, Olgaard & Brace 1983, Sammis *et al.* 1986, 1987). Early studies found that gouge particles obeyed a log-normal size distribution, and that mean particle size was inversely related to confining pressure and shear displacement (Engelder 1974, Anderson *et al.* 1980, 1983, Sammis & Osborne 1982). Based on experimental studies, Sammis *et al.* (1986) attributed the decrease in particle size with increasing confining pressure to a suppression of microfracture extension and subsequent decrease in the spacing of axial microfractures; i.e. smaller particles are produced from denser microfractures at higher pressure. Their gouge particles obeyed both log-normal and power-law size distributions.

Building on the work of Epstein (1947), Sammis *et al.*

\* Now at: Department of Geology, University of Melbourne, and CSIRO, Division of Geomechanics, Parkville Victoria, 3052, Australia.

(1986) showed that in order to produce a log-normal particle-size distribution the probability of fracture for any particle must be constant and independent of size. Such a fracture probability occurs if particle strength is independent of size. However, Sammis *et al.* (1987) rejected the idea that fracture probability is controlled by strength, after using an improved technique for studying particle-size distribution and finding a fractal (power-law) size distribution for natural gouge. They concluded that fracture probability is controlled by the relative size of nearest-neighbor particles, rather than particle strength. To explain the fractal size distribution, Sammis *et al.* (1987) proposed a model in which fracture is most likely when neighboring particles are of similar size. In this model, the distance between similar-size particles at all scales is maximized at equilibrium, producing a fractal size distribution.

Particle strength is known to vary with size (Petch 1953). Thus, an important question is what are the size limits over which particle strength is outweighed by nearest-neighbor size, and what are the factors that control these limits? In addition, how does particle-size distribution evolve with strain, and what is the role of shear-localization in comminution? We address these questions by quantifying changes in particle-size distribution as a function of shear strain and by examining the effects of shear-localization on comminution.

## EXPERIMENTAL TECHNIQUE

Using a servo-controlled triaxial apparatus, we sheared 4.0 mm thick layers of water-saturated Ottawa sand between rough steel surfaces at 45° to the axis of a cylindrical sample (Fig. 1). Ottawa sand has an average grain diameter of 400–800  $\mu\text{m}$  and is composed of >99% quartz. We sheared the gouge layer at constant effective normal stress (100 MPa) and under drained conditions (constant pore pressure,  $P_p$ , of 5 or 10 MPa). A fixed amount (9.6 g) of dry Ottawa sand was used to insure a reproducible gouge layer. To make the layers uniformly thick, we cut a polyolefin jacket along a 45° angle and extended it above the 45° surface by 4.0 mm. Gouge was then packed along the surface and saturated with water. Two additional polyolefin jackets excluded the confining medium from the layer.

We used a steel sample to avoid the complicating effects of microcracking and dilatancy adjacent to the gouge layer. To isolate the behavior of slip within gouge from effects related to the interface, ridges were machined perpendicular to the sliding direction on the steel surfaces. The ridges were 0.5 mm in height, triangular in cross-section and spaced every 0.75 mm. Normal stress across the layer was servo-controlled by using a scaled signal from an internal load cell as the servo-feedback to confining pressure. Thus, an increase in axial stress, as measured by the internal load cell, caused a simultaneous decrease in confining pressure,  $P_c$ , in a 1:1 ratio, thereby maintaining normal stress across the 45° surface. Increases in normal stress with

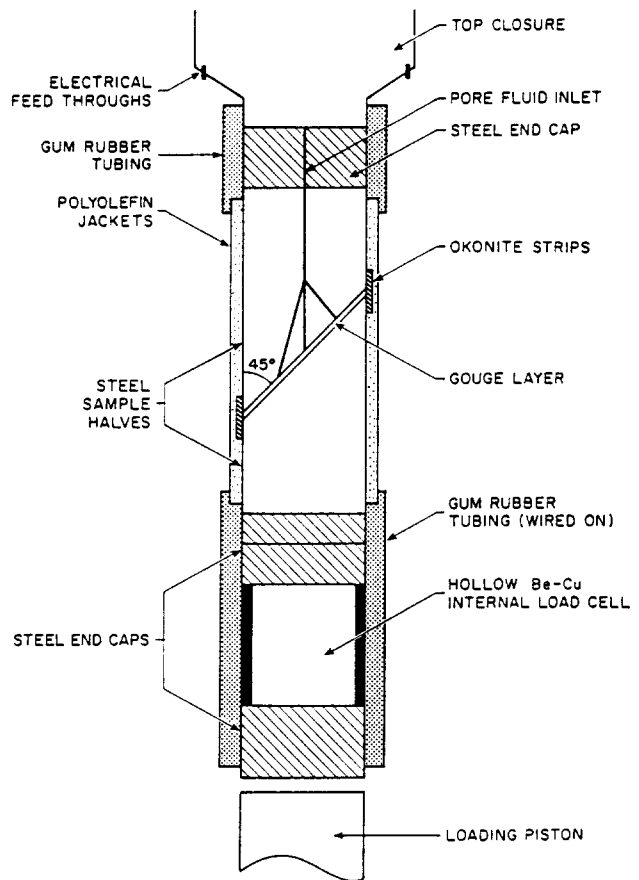


Fig. 1. Sample column assembly and set-up. Three pore-fluid access holes provided fluid communication with the gouge layer. An internal load cell was used to measure axial stress and to servo-control normal stress across the sliding surface (see text). Okonite, a soft self-vulcanizing rubber, was used between the sample and polyolefin jackets in a series of experiments to test whether a void formed with sample offset. The diameter of the steel sample, end caps and load cell is 3.5 cm. The steel sample is 8.2 cm in total length.

sample offset were not accounted for by the servo-control system, although we correct stress and porosity data for offset as described by Marone (1989). Porosity was corrected for stress increases within the central portion of the layer (due to reduced contact area with offset) and stress decreases at the ends of the layer by using the change in stress and the bulk modulus of the gouge layer (measured as  $6 \times 10^{-5} \text{ MPa}^{-1}$ ). In addition, testing with different jacketing materials and Okonite (a soft rubber) showed that a void did not form at the ends of the layer (at the position of the Okonite in Fig. 1) with offset (see Marone 1989 for details).

Pore volume changes were monitored by servo-controlling  $P_p$  at a constant value and measuring the fluid volume pumped into or out of the gouge. A volume of  $10^{-5} \text{ cm}^3$  could be resolved. Three pore fluid access holes were used (Fig. 1) to allow fluid communication with the gouge layer. To check whether the pore pressure remained constant during loading, we ran tests in which shear displacement was periodically stopped and pore volume change was monitored. In all cases the lag between halting displacement and zero pore volume change was less than 1–2 s. In addition, the load-cycling experiments provided a check for pore fluid communi-

cation. At sufficiently fast displacement rates ( $>70 \mu\text{m s}^{-1}$ ), porosity lagged displacement on the transition from loading to unloading. That is, in the case of dilatancy during slip, fluid continued to flow into the layer after slip had stopped and unloading had commenced. Thus, we used displacement rates of  $\leq 30 \mu\text{m s}^{-1}$  and in all cases the porosity and displacement 'turn-around' were simultaneous at our digital sampling interval of 0.5 s.

The initial porosity of the gouge layer prior to loading was  $34 \pm 1\%$ , as determined by weighing dry and saturated gouge layers. To estimate absolute porosity under load, we assumed 34% porosity at 0.5 MPa effective pressure ( $P_c = 10.5 \text{ MPa}$  and  $P_p = 10 \text{ MPa}$ ) and measured pore volume change during hydrostatic loading. These measurements indicate that porosity was  $18 \pm 1\%$  at 100 MPa effective hydrostatic pressure, prior to shear strain. For comparison between experiments, we assume porosity was 18% at  $\gamma = 0$  in the figures that follow.

Displacement across the sliding surface was measured with a linear variable differential transformer (LVDT) mounted external to the pressure vessel on the axial ram, and is reported here as shear strain. Shear displacement ( $\delta u$ ) was derived from axial displacement using the angle of the sliding surface and a correction for elastic shortening within the piston and sample column. Shear strain ( $\gamma$ ) was calculated as  $\gamma = \delta u/d$ , where  $d$  is the

initial gouge thickness (4.0 mm). We used displacement rates of  $0.1\text{--}30.0 \mu\text{m s}^{-1}$  as measured along the axial ram (shear strain rates of  $3.5 \times 10^{-5}\text{--}1.1 \times 10^{-2} \text{ s}^{-1}$ ). All data were recorded digitally at a sampling interval of 0.05–5.0 s, depending on displacement rate.

## RESULTS

### Mechanical behavior

Figures 2–5 show the basic mechanical and porosity data recorded during this series of experiments. A list of the experiments is given in Table 1.

Single-cycle experiments (Fig. 2) exhibited strain hardening and compaction for shear strains,  $\gamma$ , of less than 0.8, after which dilatancy was observed and the rate of strain hardening decreased. Compaction occurred upon unloading and the final porosity,  $\phi$ , increased with strain for  $\gamma > 0.8$ ; i.e. the dilatant volume increase during slip was not fully recovered upon unloading. The lowest porosities reached in single-cycle experiments were 10–11%. Comparison of the curves shown in Fig. 2 shows experimental reproducibility.

In multiple-cycle experiments (Figs. 3 and 4) the axial ram was repeatedly advanced, causing an increase in shear stress, and then retracted until the shear stress returned to zero. During the initial increments of shear,

Table 1. A suite of single and multiple cycle experiments to successively greater shear strain. All but one of the experiments were at 100 MPa normal stress. The gouge layers were epoxy impregnated and examined for microstructures; a yes (y) is recorded under  $R_1$  shears (see text) if at least one distinct  $R_1$  feature was observed within that layer (n = not observed)

Experiment	Shear strain	$R_1$ shears	Fractal dimension $D$	Intercept at 0.1 mm 50× ( $\text{mm}^{-2}$ )
Single cycle				
GSA09C	0.00	n	1.68	0.77
GSA05C	0.10	n	1.94	0.74
GSA11C	0.50	n	2.34	0.97
GSA10C	0.74	n	2.14	1.02
GSA08C	1.00	n	2.46	1.09
GSA07C	1.49	y	2.40	1.16
GSA00C	2.01	y	2.49	1.06
GSA06C	2.19	y	2.72	1.06
GSA01C	2.50	y	2.70	1.16
GSA04C	3.30	y	2.49	0.92
GSA12T (20 MPa)	2.30	n	2.40	1.12
Multiple cycle				
GS03C	0.00	n	1.87	0.83
GS01C	0.20	n	2.23	0.92
GS02C	0.27	n	2.01	0.96
GS04C	0.40	n	2.25	1.16
SG36C	0.40	n	2.24	0.97
GS05C	0.60	n	2.32	1.14
GS07C	1.10	n	2.28	1.15
SG38C	1.30	y	2.63	1.10
GS11C	1.34	y	2.57	1.10
SG32C	1.50	y	2.62	1.16
GS08C	1.60	y	2.81	1.15
SG35C	1.69	n	2.52	0.96
SG31C	1.70	y	2.61	1.11
SG37C	2.35	y	2.83	0.97
SG34C	2.88	y	2.62	1.10

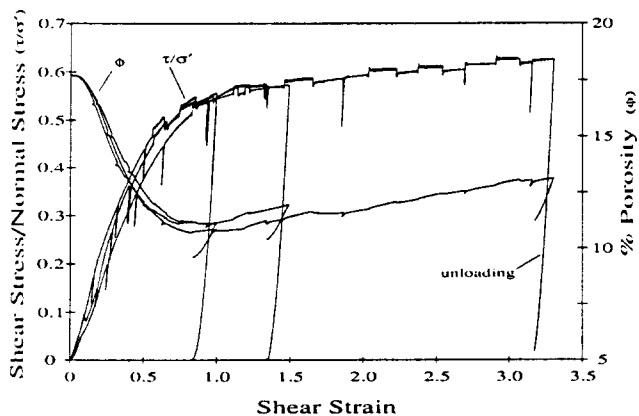


Fig. 2. Normalized shear stress and porosity vs shear strain for three single-cycle experiments sheared to progressively greater strain. Compaction and strain hardening occurred for the initial increments of strain. After a shear strain of 0.8, dilatancy occurred along with a transition from rapid to slow strain hardening. Unloading caused compaction. The shear stress and porosity curves contain variations due to changes in shear-displacement rate, which are the subject of another study (Marone *et al.* in review), as well as short periods of unloading (the near-vertical lines), which were used to monitor variations in stiffness.

compaction occurred upon both loading and unloading. After a strain of 0.2–0.4, dilatancy was observed upon loading. At  $\gamma = 0.8\text{--}0.9$  the dilatant increase in porosity upon loading became about equal to the porosity decrease upon unloading, resulting in a steady porosity level (as measured at hydrostatic pressure) of 7–8% (Fig. 3b). This porosity level persisted for relatively short-displacement cycles as in Fig. 3(b).

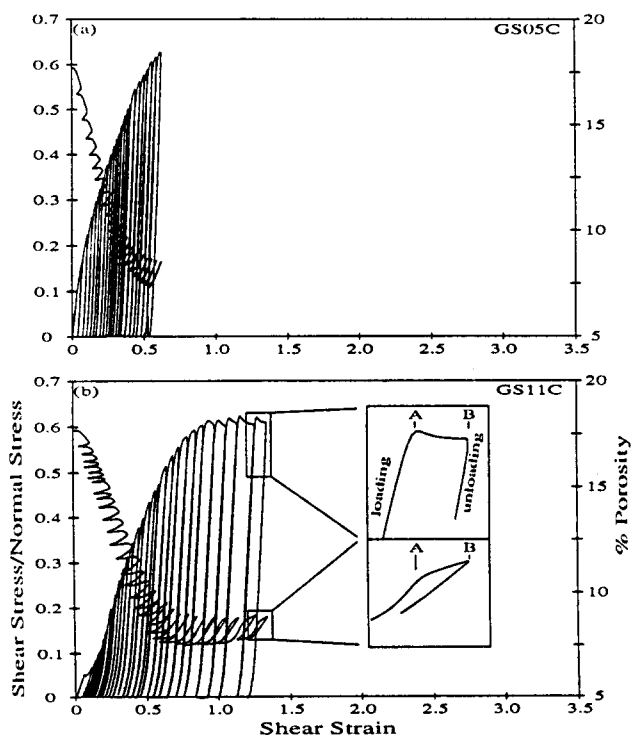


Fig. 3. Normalized shear stress and porosity for multiple-cycle experiments. In these experiments the sample was loaded and unloaded (inset) in arbitrarily defined cycles. Compaction and strain hardening occurred during the initial increments of shear. After a shear strain of 0.2–0.4 dilatancy occurred upon loading followed by compaction during yield.

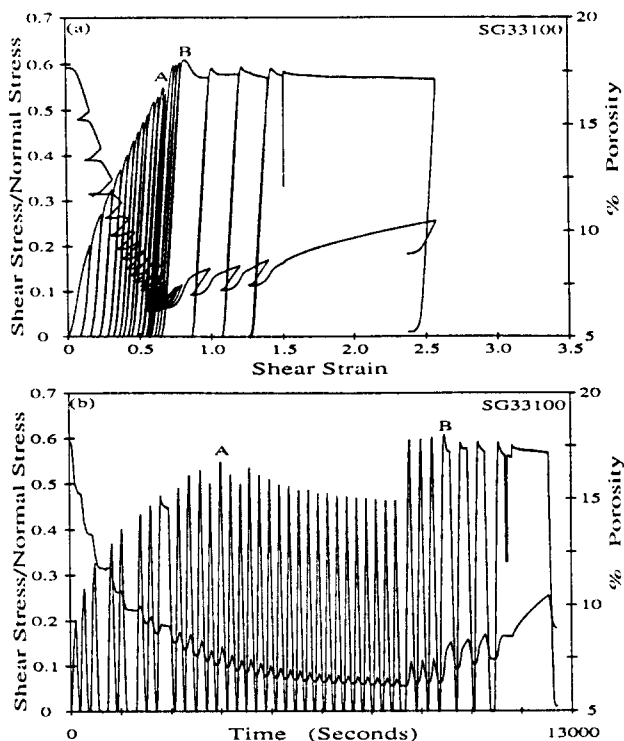


Fig. 4. Normalized shear stress and porosity vs shear strain (a) and time (b) for an experiment in which the shear load was cycled repeatedly without significant net slip (A–B) followed by long-displacement cycles. Note porosity reduction with load cycling from A to B. Cycles with little net slip resulted in compaction, whereas cycles with significant offset produced net dilation. (See text for further explanation.)

Figure 4(a) illustrates the effect of repeated cycling without significant slip (A to B) followed by cycles that exhibit a peak stress and significant inelastic slip; hereafter referred to as long-displacement cycles. The data in Fig. 4(a) are plotted vs time in Fig. 4(b) in order to show the details of each cycle. Cycling of the shear load without significant slip resulted in net compaction, and porosity asymptotically approached 5.5–6% (Fig. 4b). Long-displacement cycles then resulted in net dilation. The first cycle following net compaction (B in Fig. 4) showed a higher peak stress and larger volume increase than subsequent cycles, each of which exhibited net dilatancy proportional to its total slip. As discussed below, an exaggerated peak stress and net volume increase indicate overconsolidation (i.e. a lower porosity than the equilibrium porosity for a given normal load; Lambe & Whitman 1968).

In multiple-cycle experiments, the dilatancy rate,  $d\phi/d\gamma$ , during loading of a given cycle increased with cycling from  $\gamma = 0$  to 0.8 after which it was about constant (Fig. 5a). In a typical cycle, the dilatancy rate first increased with strain and then decreased (Fig. 5b). We computed  $d^2\phi/d\gamma^2$  directly from the digital data. The dashed line in Fig. 5(b) indicates that  $d^2\phi/d\gamma^2$  became negative at about the peak stress. As pointed out by Frank (1965) and discussed below, the transition from positive to negative  $d^2\phi/d\gamma^2$  results in a shear localization condition. In multiple-cycle experiments, porosity–strain curves began to show a distinct inflection

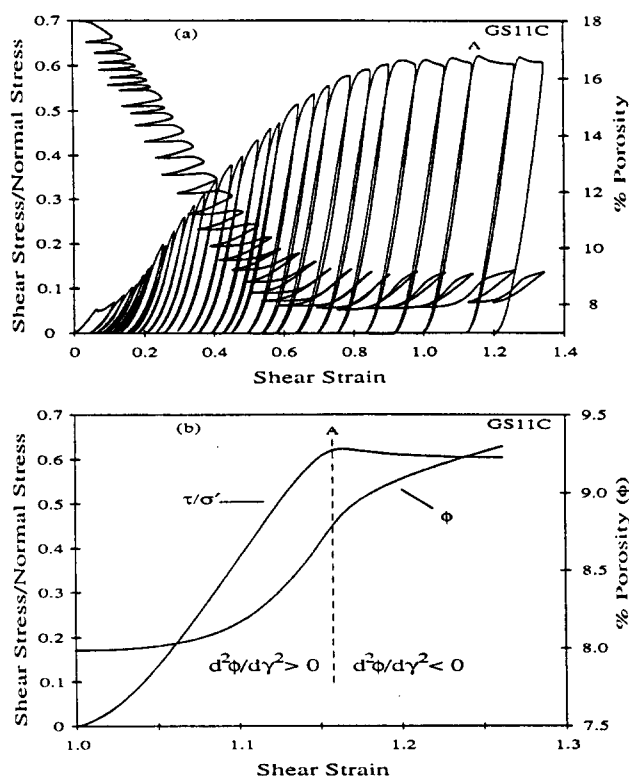


Fig. 5. (a) An enlargement of the experiment shown in Fig. 3(b). The dilatancy rate,  $d\phi/d\gamma$ , as measured just prior to the peak stress (see b) increased with each cycle from  $\gamma = 0$  to 0.8, after which it was roughly constant with additional cycling. (b) An enlargement of the cycle marked A, which starts at  $\gamma = 1.0$  in (a). Note that  $d^2\phi/d\gamma^2$  changes from positive to negative at about the peak stress and that the porosity-strain curves in (a) begin to show a distinct inflection in  $d^2\phi/d\gamma^2$  at  $\gamma = 0.8-0.9$ .

in  $d^2\phi/d\gamma^2$  at  $\gamma = 0.8-0.9$  (Fig. 5b). Single-cycle experiments show negative  $d^2\phi/d\gamma^2$  after  $\gamma = 0.8-1.0$ .

#### Comminution and microstructures

Following each experiment, the deformed gouge layers were carefully removed from the steel samples and impregnated under vacuum with a low-viscosity epoxy. The exopied layers were thin-sectioned along planes parallel to the slip direction and perpendicular to the plane of the layer. Each section was polished with successively finer grit, starting with #600 and finishing with  $0.05 \mu\text{m}$  alumina. We examined the sections using optical and scanning electron microscopes (SEM).

To illustrate the nature of comminution and particle size reduction within different gouge layers, we show a series of backscattered-electron SEM images at different magnifications in Figs. 6–8. The higher-magnification photos were taken from within the field of view at the next lowest magnification. Thus, the  $200\times$  field of view in Fig. 6(c) is present within each of Figs. 6(b) & (a), and so on.

Gouge layers subjected to hydrostatic load but not shear (Fig. 6) contain significantly fewer small particles than sheared gouge layers (Figs. 7 and 8). Particles within hydrostatically loaded layers have irregular 'moth-eaten' edges at all scales, and show fracture

primarily along their edges. Small particles are commonly elongate slivers produced by spalling and fracture at the edges of larger particles (Fig. 6). Sheared layers contain both thoroughly fractured particles and particles free of fractures (Figs. 7 and 8). As observed previously by Sammis *et al.* (1987) for natural gouge, particles without fractures do not have similar-size nearest neighbors (i.e. the largest particles in Fig. 8a) or one of the particles has just been crushed (e.g. Fig. 7a). Figure 7(a) also shows one of the principal mechanisms of comminution, in which one grain, pinned between two similar-size neighbors, has been crushed in place. The larger particles within the sheared layers have irregular edges (Figs. 7a and 8a & b), similar to those found in hydrostatically stressed layers, whereas smaller particles from the sheared layers have less jagged edges (compare Figs. 7a & b and Figs. 6c and 7b). Layers subjected to single-cycle (Fig. 8) and multiple-cycle shear loading (Fig. 7) show about the same degree of comminution.

Oblique (Riedel) shears form at  $\gamma = 1.3-1.5$  (see Table 1) in both single and multiple-cycle experiments. These shear bands occur at  $15 \pm 3^\circ$  to the plane of the gouge layer (Figs. 9a & c) and are therefore parallel to the  $R$  shears described by Tchalenko (1970) in clays or the  $R_1$  shears described by Logan *et al.* (1979) in simulated gouge. Riedel shear structures are observed for shear within smoother surfaces (i.e. rock surfaces ground with #60–#80 grit, which produces an r.m.s. roughness of  $10-20 \mu\text{m}$ ; e.g. Byerlee *et al.* 1978, Logan *et al.* 1979) than our steel surfaces, and thus the development and angle of Riedel shear bands is apparently not affected by surface roughness over the range from a few microns to a few mm r.m.s. roughness. Our shear bands are characterized by particle-size reduction (Fig. 9b) and a thin linear void space, which is possibly caused by or accentuated by epoxy impregnation. Shear bands occasionally occur in pairs as in Fig. 9(a). Our layers also contain conjugate localization features at a high angle to  $R_1$  shears, such as the  $X$  shears described by Logan *et al.* (1979). However, these are not as well developed as the  $R_1$  features. In addition, boundary shears (parallel to the  $Y$  shears of Logan *et al.* 1979) are present at the gouge-steel interface as indicated by streaks along the surfaces of the gouge layer (Fig. 9c). The streaks indicate slip between the gouge layer and a thin layer of fine particles held within the grooves in the steel surfaces. Boundary shear is clearly limited to one half of each interface (Fig. 9c), as indicated by an impression of the steel sample's grooves on the other half of the gouge surface.

The above data are all from experiments at 100 MPa normal stress, which is above the crushing strength of individual quartz grains (55–60 MPa, as indicated by an abrupt increase in the rate of porosity reduction during hydrostatic loading). Although it is clear from the data shown in Figs. 6–8 that shear displacement promotes grain size reduction, it is not clear what effect normal stress has on the mechanisms of fracture (e.g. tensile splitting, spalling) and comminution. We therefore ran an experiment at 20 MPa normal stress and to  $\gamma = 2.3$ . The 20 MPa gouge (Figs. 9d & e) shows fewer fractures

within particles of all sizes than 100 MPa gouges deformed to similar strains. In addition, a careful look at the particles in Figs. 9(d) & (e) (note the edges of the larger particles) reveals that spalling is the dominant mechanism of size reduction, as opposed to grain crushing (e.g. Fig. 7a).

#### Particle-size analysis

We measured the two-dimensional particle-size distribution of our gouge layers using the counting method described by Sammis *et al.* (1987) and SEM images such as in Figs. 6–8 and 9(d) & (e). This method has a considerable advantage over sieve techniques in that it preserves the spatial relationships between particles and does not involve additional fracturing, as may occur during sieving. We used an image analyser (Lemont Scientific Inc., model DV-4400) to automatically measure, count and sort particles by area-equivalent

diameter; i.e. the diameter of a circle with an area equivalent to that calculated by direct measurement. Backscattered-electron SEM images were necessary because conventional reflected-light microscope images did not have sufficient contrast for the image analyser to accurately identify particles.

For each gouge layer we took photographs at 50, 200 and 800 $\times$  and, following Sammis *et al.* (1987), sorted particles into bins that decreased in size by a factor of two (Table 2). We set the upper size limit at 800  $\mu\text{m}$  to include the size of our starting material and the lower limit at 1.5625  $\mu\text{m}$ . 800 $\times$  photographs were not taken when, in cases such as Fig. 6, the 200 $\times$  photographs contained few small particles.

Previous studies of natural and experimentally-produced gouge have found either log-normal (e.g. Engelder 1974, Sammis & Osborne 1982, Sammis *et al.* 1986, Yoshioka 1986) or power-law (Sammis *et al.* 1987, Biegel *et al.* 1989) particle-size distributions. We find

Table 2. Particle densities,  $N(n)/A$ , where  $N(n)$  is the number in size range  $n$  and  $A$  is the area of the photographs, for the photographs in Figs. 6–8 and 9(d) & (e). The data are plotted in Fig. 10 which shows our method for determining the fractal dimension  $D$ .

Area-equivalent diameter (mm)	Number per area (mm <sup>-2</sup> )		
	Photo#–Mag.		
GSA09C (Fig. 6)	106–25 $\times$	107–50 $\times$	108–200 $\times$
0.400–0.800	4.36	7.41	
0.200–0.400	2.82	3.37	
0.100–0.200	1.45	5.05	11.8
0.050–0.100	0.91	1.01	35.5
0.025–0.050	0.18	0.67	23.7
0.0125–0.025			0.00
0.00625–0.0125			11.8
SG38C (Fig. 7)	97–50 $\times$	98–200 $\times$	99–800 $\times$
0.400–0.800	0.97		
0.200–0.400	2.26		
0.100–0.200	5.81	0.00	
0.050–0.100	17.4	26.3	
0.025–0.050	41.6	147.4	84.0
0.0125–0.025		594.8	1260.5
0.00625–0.0125		1094.8	1428.6
0.003125–0.00625			2184.9
0.0015625–0.003125			2184.9
GSA07C (Fig. 8)	134–50 $\times$	135–200 $\times$	136–800 $\times$
0.400–0.800	0.34		
0.200–0.400	1.01		
0.100–0.200	8.08	5.92	
0.050–0.100	24.9	71.0	
0.025–0.050	77.4	171.6	471.7
0.0125–0.025		289.9	566.0
0.00625–0.0125		562.1	1226.4
0.003125–0.00625			2735.9
0.0015625–0.003125			7264.1
GSA12T (Fig. 10)	249–50 $\times$	250–200 $\times$	
0.400–0.800	0.67		
0.200–0.400	1.35		
0.100–0.200	8.08	5.92	
0.050–0.100	24.6	47.3	
0.025–0.050	70.4	130.1	
0.0125–0.025		278.1	
0.00625–0.0125		503.0	

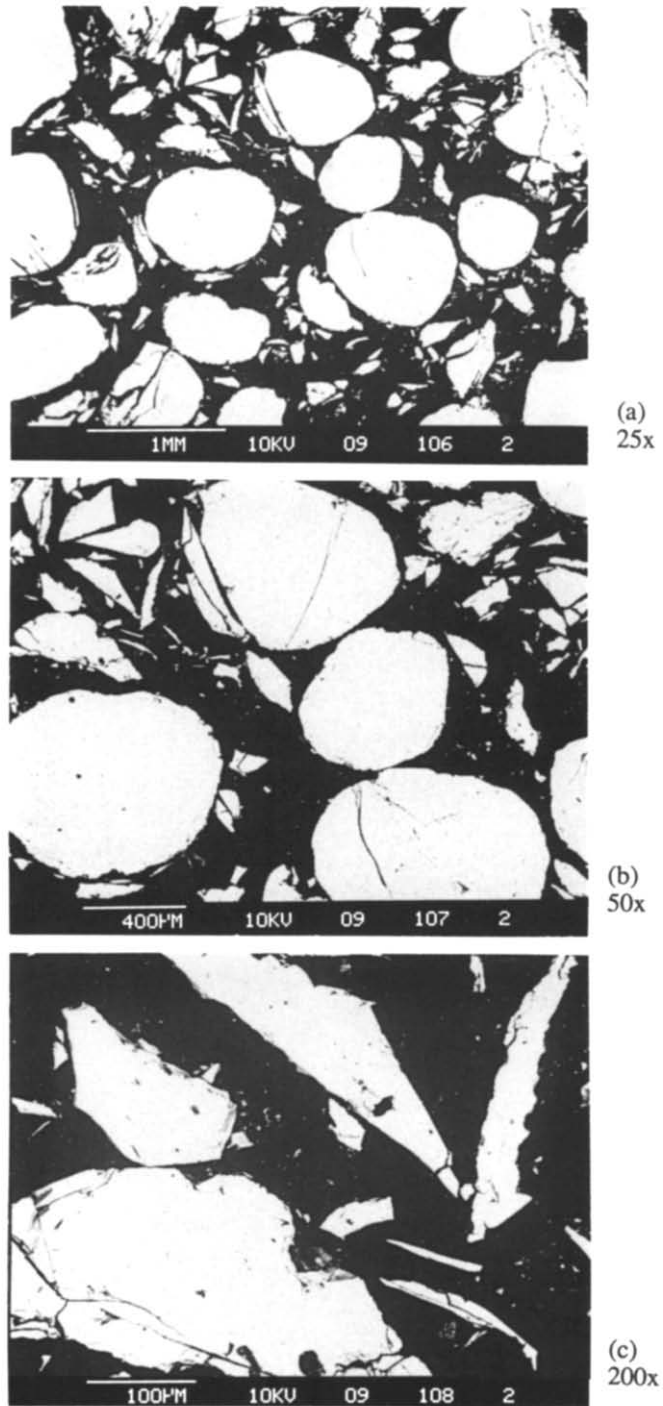


Fig. 6. Backscattered-electron SEM images at 25, 50 and 200 $\times$  of a gouge layer (GSA09C) subjected to 100 MPa hydrostatic load. The photograph is of a section oriented parallel to the slip direction and perpendicular to the plane of the gouge layer; thus normal stress acted in a vertical direction. Here and in the following figures quartz particles and epoxy are white and black, respectively. The largest grains at 25 $\times$  represent the size of original Ottawa sand grains. Note the lack of small grains in all photographs compared with similar magnification photographs in Figs. 7 and 8.

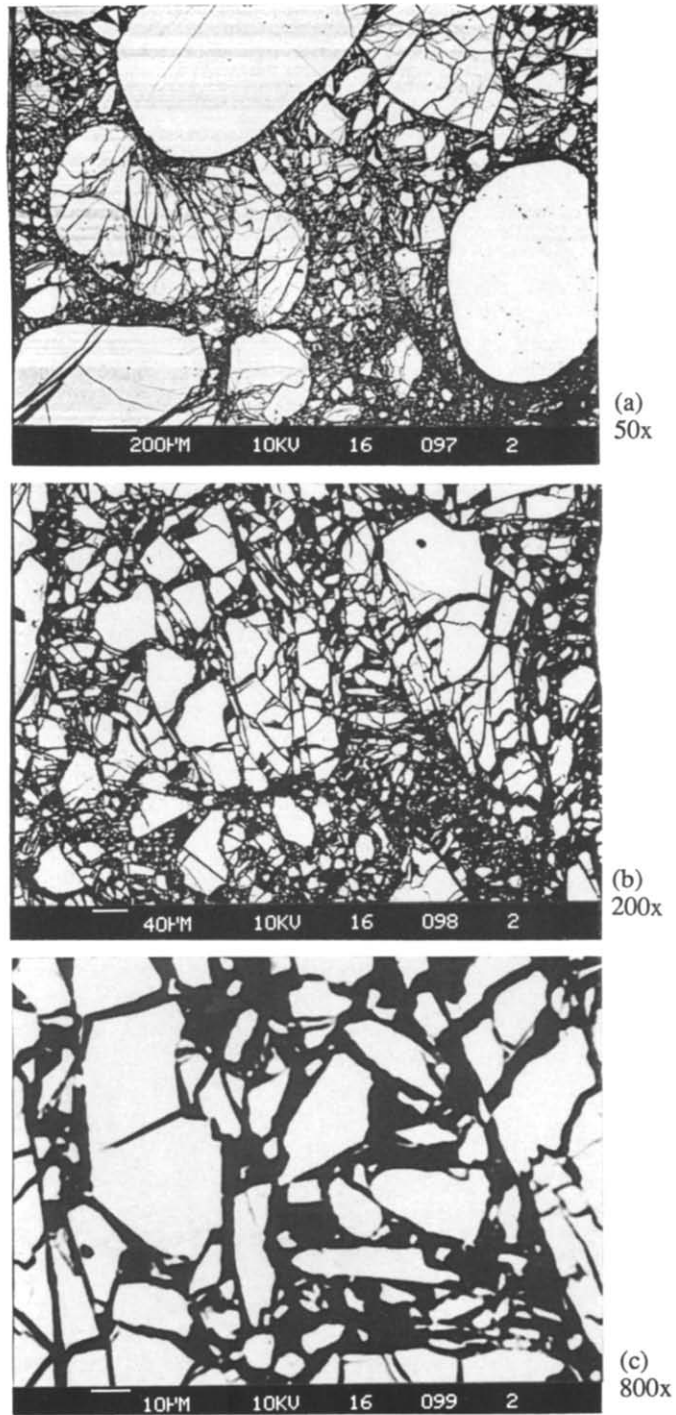


Fig. 7. 50, 200 and 800 $\times$  photographs of a gouge layer (SG33C) deformed by load cycling at 100 MPa to  $\gamma = 1.3$ . Note impingement and crushing of similar-size particles in (a). Note the lack of 'smaller' grains in (c), whereas in (a) and (b) 'small' grains make up the background.



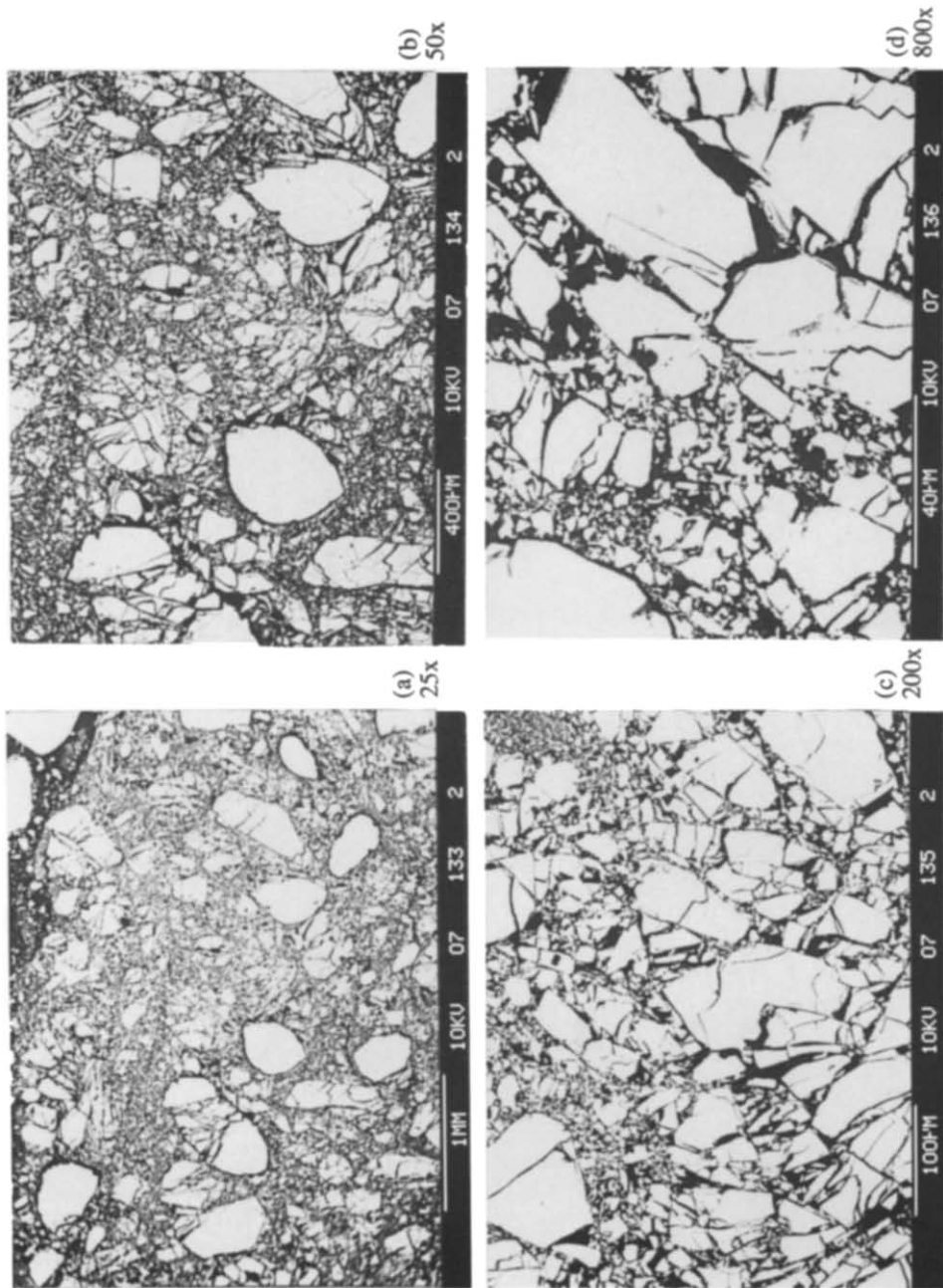


Fig. 8. 25, 50, 200 and 800 $\times$  photographs of a gouge layer (GSA07C) deformed in a single-load cycle at 100 MPa and  $\dot{\epsilon} = 1.5$ . Smaller particles are present in the background at each scale. Note the relic particle in the center of (b), and that the largest particles in (a) are significantly smaller than those in Fig. 6(a).

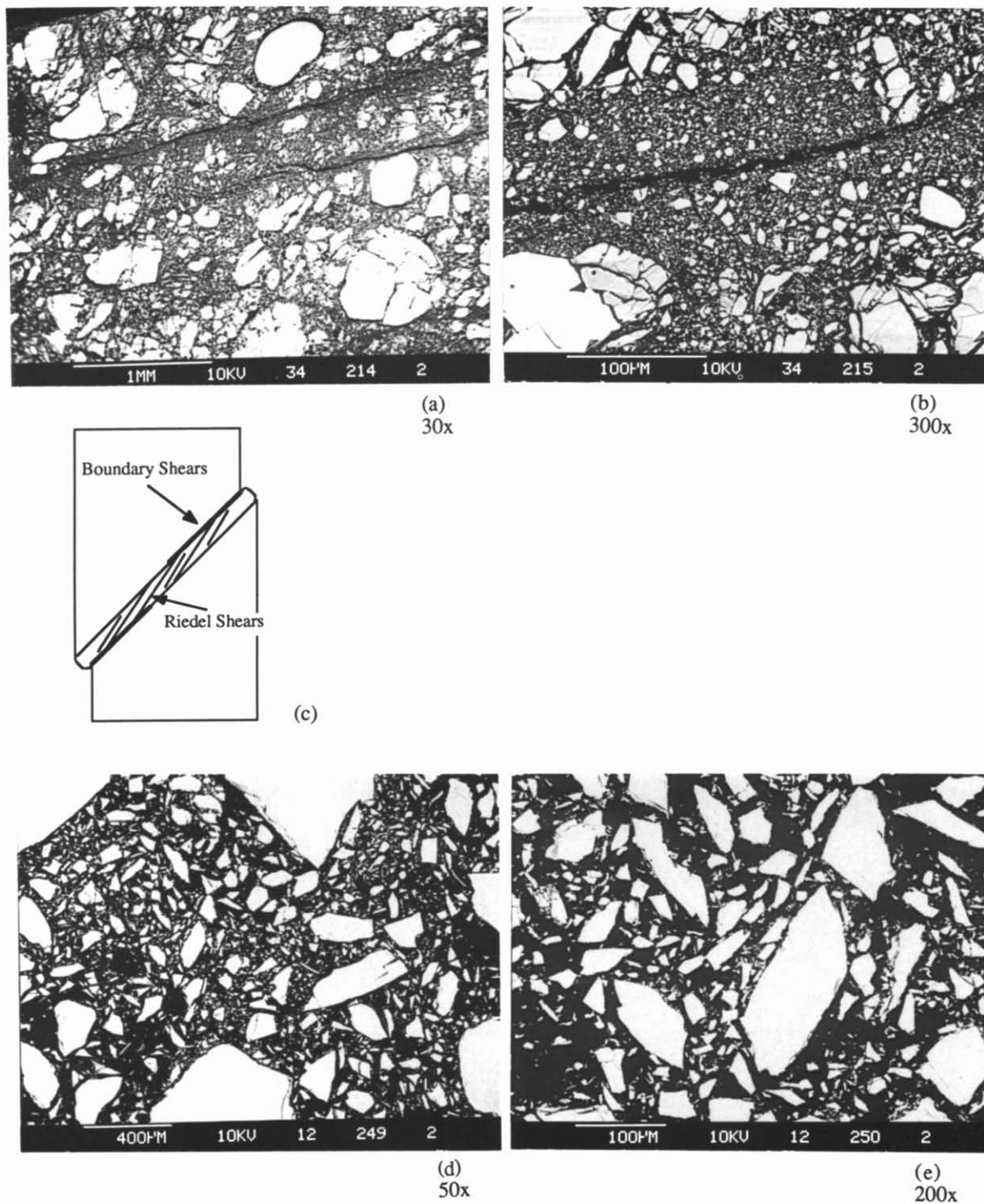


Fig. 9. (a & b) SEM photographs showing oblique (Riedel) shear bands. The gouge layer boundaries are horizontal in each photograph and the sense of shear is sinistral. (a) 30 $\times$  view of a layer subjected to  $\gamma = 2.9$ . (b) 300 $\times$  view of the upper shear band in (a). Note sharp boundaries and particle-size reduction within the shear band. (c) Illustration of the sample and gouge layer, showing the prominent microstructures. Note that boundary shears do not extend over the entire length of the interface. (d & e) 50 and 200 $\times$  photographs of a gouge layer (GSA12T) deformed at 20 MPa to  $\gamma = 2.3$ . Few intragranular fractures are present compared with the 100 MPa cases shown in Figs. 6–8. Spalling of large particles produced small fragments and fractures at the edges of larger particles.

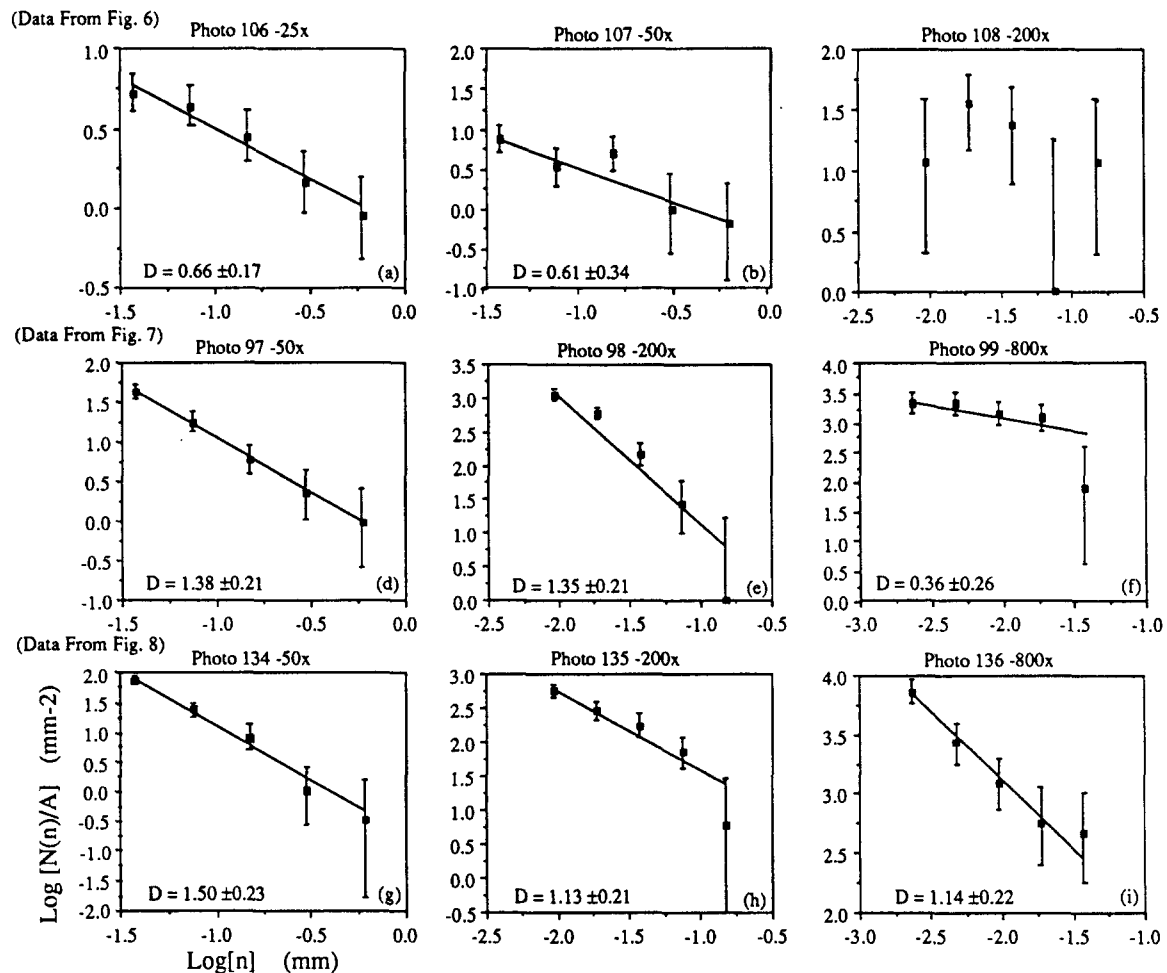


Fig. 10. Particle densities (the number in a size range per photograph area) vs the mean of each size range for the photographs in Figs. 6–8. See Table 2 for size ranges. The fractal dimension of the particle-size distribution,  $D$ , is calculated from a weighted least-squares fit to each distribution, and reported along with the standard deviation. The error bars represent 95% confidence limits for  $N(n)$ , on the assumption that we are sampling (counting) a Poissonian spatial distribution (see Wilson 1952, p. 191). The lower fractal limit is  $6.25\text{--}12.5\ \mu\text{m}$  for (d–f) and  $\leq 1.5\ \mu\text{m}$  for (g–i). Note that the lower fractal limit for Fig. 7 ( $6.25\text{--}12.5$ ) falls within the  $800\times$  photograph and thus confirms the qualitative difference between Fig. 7(c) and Figs. 7(a) & (b); i.e. that there are proportionally more ‘small’ particles in Figs. 7(a) & (b).

that our data is best fit with a power-law distribution such as given by

$$N(n)/A = b n^{-D}, \quad (1)$$

where  $N(n)$  is the number of particles in a size range,  $A$  is the area examined,  $n$  is the mean of the size range, and  $b$  and  $D$  are constants. Equation (1) also defines a fractal distribution (Mandelbrot 1982) with fractal dimension  $D$ . A fractal set is one in which the size–frequency relation is independent of scale over an infinite range. For a distribution with finite range, the upper and lower fractal limits are defined as the limits over which the distribution obeys a scale-independent size–frequency relation.

To evaluate the effects of shear strain and load cycling, we characterized each of our gouge layers by calculating the fractal dimension of the particle-size distribution. To calculate  $D$ , we used a weighted least-squares fit to  $\log(N(n)/A)$  vs  $\log(n)$  (Fig. 10). The weights provide a quantitative means of having greater confidence in points based on a larger number of counts (Fig. 10). Weights,  $w$ , were calculated for each point

using a standard relation,  $w = \sigma^{-2}$ , where  $\sigma$  is the standard deviation. We computed the standard deviation on the assumption that we sampled (counted) a Poissonian spatial distribution of particles (see Wilson 1952, p. 191). In general, weighted least-squares fit the mean of each point within one standard deviation. For comparison, the  $25$  and  $50\times$  photographs in Fig. 6 were analyzed for the same size range. They show good agreement (Fig. 10a & b).

We also calculated the intercept ( $b$ ) at  $0.1\ \text{mm}$  for the  $50$  and  $200\times$  cases. However, the intercept is not a useful parameter for comparison between photos since the site for each photo is not chosen at random. This can be understood with reference to Fig. 8. The sites for higher-magnification photos were chosen so as to exclude particles larger than the maximum size at that magnification (see Table 2). As discussed by Sammis *et al.* (1987), this does not affect the relative number of particles in different size ranges, but it imposes a scale on the distribution and results in adding an arbitrary constant to the number counted in each size range. Thus site selection adds an arbitrary constant to the  $y$ -intercept in

Fig. 10. This means data from different photos cannot be combined directly to calculate the overall size distribution, but rather the distributions have to be calculated individually for each photo and the values of  $D$  combined.

The problem of generalizing data from a two-dimensional section to a three-dimensional volume is discussed by Underwood (1968) and Sammis *et al.* (1987). In the case of the fractal dimension the three-dimensional  $D$  is simply the two-dimensional  $D$  plus 1;  $D_{3-d} = D_{2-d} + 1$  (Mandelbrot 1982). We use the three-dimensional  $D$  in what follows.

The upper and lower fractal limits are defined for our distributions as the limits within which particles obey a fractal size distribution. For our layers, the upper fractal limit is  $800 \mu\text{m}$ , since the lowest magnification photographs obey a fractal distribution (Fig. 10a, d & g). The lower fractal limit varies from layer to layer. Layers subjected to hydrostatic load show lower fractal limits of  $25\text{--}50 \mu\text{m}$  (Fig. 10a-c), whereas sheared layers have lower fractal limits of  $<25 \mu\text{m}$  (Figs. 10d-f & g-i). The lower fractal limit varies inversely with total shear strain, indicating increasing comminution with shear.

Because of the differences in lower fractal limits, and in order to compare the distributions of different gouge layers over the same size range, we restricted the size range to  $12.5\text{--}800 \mu\text{m}$  when computing  $D$ . Values of  $D$  obtained from 50 and 200 $\times$  photographs were averaged to derive a  $D$  for each layer. In general, the 50 and 200 $\times$  values agree within one standard deviation as determined from the weighted least-squares fit.

For gouge layers subjected to 100 MPa hydrostatic load, the fractal dimension of the particle size distribution,  $D$ , is  $1.8 \pm 0.15$  (Fig. 11). Within the bulk material, away from the  $R_1$  shears,  $D$  increases with strain for  $\gamma < 1.3\text{--}1.7$ .  $D$  shows similar shear strain dependence for single and multiple cycle experiments, and thus at a given strain  $D$  is similar for the two sets of experiments. In each case,  $D$  undergoes a rapid initial increase and levels off to an asymptotic value of  $2.62 \pm 0.15$  by  $\gamma = 1.3\text{--}1.7$  (Fig. 11). The steady state values of

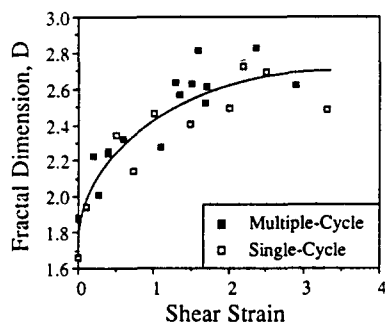


Fig. 11. Fractal dimension  $D$  vs shear strain for the single- and multiple-cycle experiments at 100 MPa. The values of  $D$  are given in Table 1.  $D$  increases with strain up to 1.3–1.5 and levels off to an asymptotic value thereafter. Single- and multiple-cycle experiments show similar particle-size distributions. The errors in the individual values of  $D$ , which may be calculated from the maximum and minimum slope consistent with the 95% error bars, are on the order of the scatter between points at similar strains. The curve is positioned by eye.

$D$  (i.e. for  $\gamma >$  about 1.5) are equivalent to those predicted by the Sammis *et al.* (1987) comminution model.

The particle-size distribution at 20 MPa has a fractal dimension of 2.40 and is therefore comparable (for the size range  $12.5\text{--}800 \mu\text{m}$ ) to the 100 MPa experiments deformed to similar strains. Thus, although the lower fractal limit and mean grain size are clearly larger for the 20 MPa experiment (compare Figs. 9d & e with Figs. 7 and 8), the relative proportion of large and intermediate grains is about the same.

Given the important role shear localization plays in shear zone development, it is of interest to ask whether the particle-size distribution differs within and outside shear bands. We therefore made a series of photos at 300 $\times$  to compare particle-size distributions for the bulk material and the  $R_1$  shear bands. We were unable to study particles within the boundary shears since they were only partially preserved when the gouge layers were removed from the steel samples. The  $R_1$  shear bands range from 100 to 200  $\mu\text{m}$  in width and 300 $\times$  photographs were chosen so as to include their entire width. In a case such as that shown in Fig. 9(b), areas outside the shear band boundaries were not counted as part of the shear band and the area of the photograph was adjusted accordingly. 300 $\times$  photographs were also taken in the areas adjacent to the shear bands in order to make a direct comparison. Several photographs were made along the length of a given shear band and within the surrounding material and, in each case, the photographs were analyzed for grains between 6.25 and 100  $\mu\text{m}$ .

A comparison of the particle densities,  $N(n)/A$ , for areas within and outside four shear bands is given in Fig. 12. Although such a comparison is hindered by photograph-site selection, as discussed above, the constant added to each size range should be random and therefore the effect should average-out for several sets

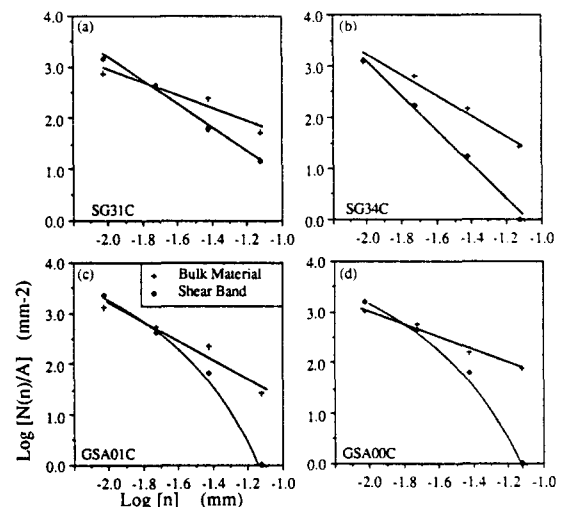


Fig. 12. Comparison of the particle densities (number per area) for particles within the bulk material and shear bands. The size ranges are  $6.25\text{--}12.5$ ,  $12.5\text{--}25$ ,  $25\text{--}50$  and  $50\text{--}100 \mu\text{m}$ . In each case there are fewer large particles and an equal or greater number of small particles in the shear bands compared with the bulk material.

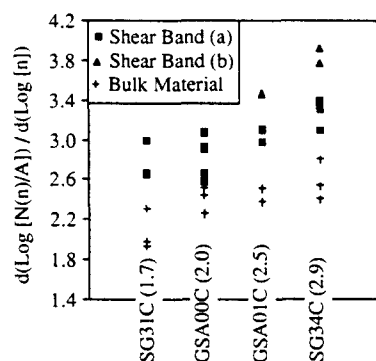


Fig. 13. Comparison of particle-size distributions for particles within shear bands and the bulk material. For each layer the sample number and total strain are given on the abscissa. Two separate shear bands were studied in three layers and these are marked (a) and (b). The shear bands have a higher slope for log particle density vs log size, indicating proportionally more small particles than for the bulk material. The slope for the shear bands increases with shear strain.

of photographs. Shear bands had significantly fewer large particles than the bulk material (Fig. 12), in agreement with the qualitative observation of reduced mean particle size within shear bands (Fig. 9b). The upper fractal limit for particles within shear bands was 25–50  $\mu\text{m}$  (Fig. 12), whereas the upper fractal limit for the bulk material was 800  $\mu\text{m}$ . Thus, the particles within shear bands do not follow a fractal size distribution for the range studied. However, for the purposes of comparison we calculated the slope of  $\log(N(n)/A)$  vs  $\log(n)$ . Particle-size distributions within shear bands have consistently higher slopes than for the bulk material (Fig. 13). In addition, the slope of the particle-size distribution for shear bands increases with increasing strain (Fig. 13), in contrast to that of the bulk material, which levels off to an asymptotic value (Fig. 11). This suggests that after development of the shear bands, subsequent comminution is localized within the gouge layer.

## DISCUSSION

### Porosity changes during shear

Porosity reduction within granular materials may occur by either an increase in packing (i.e. a better fit between particles and thus decreased void space) or by a change in particle-size distribution (sorting). For less sorted material, the range of sizes is larger and smaller particles fit between larger ones, reducing pore space. The degree of sorting can be described with the sorting coefficient,  $S_0$ , which is a measure of the size range of the distribution.  $S_0 = (Q_1/Q_3)^{0.5}$ , where  $Q_1$  and  $Q_3$  are the larger and smaller quartiles of the distribution, respectively (Krumbein & Sloss 1951, p. 100). Distributions with a greater size range have larger  $S_0$  or 'poorer' sorting. In our gouge layers, changes in sorting occur via particle-size reduction and comminution.

Cyclic shear loading is the most effective way to reduce porosity in a granular material (Youd 1972). As Youd pointed out, distortion is necessary to allow grains

to attain a more compact structure and, although hydrostatic loading can produce distortion or crushing during the first loading cycle, repeated cycles of hydrostatic loading produce negligible additional volumetric strain. Crushing is negligible at the pressures used in soil mechanics experiments (<200 KPa), hence porosity reduction occurs primarily via increased packing. At higher pressures, as in our experiments, porosity reduction may also occur via fracture and an increase in sorting coefficient. Rogers & Head (1961) showed that porosity decreases continually with increasing  $S_0$ . Thus, during comminution, as long as some large grains are preserved,  $S_0$  will increase and porosity will decrease as smaller particles fill yet smaller voids. However, if the particles become *uniformly* small,  $S_0$  will decrease and porosity will increase.

In our single-cycle experiments, compaction occurs from  $\gamma = 0$  to 0.8 (Fig. 2) together with changes in the particle-size distribution (Fig. 11). Thus, an increase in sorting coefficient is the primary cause of compaction. Multiple-cycle experiments also undergo a change in particle-size distribution during this stage, however, they show approximately 50% more compaction than single-cycle experiments. The similarity in particle-size distribution for the two types of experiments (Fig. 11) indicates that additional compaction in multiple-cycle experiments is the result of increased packing, since a change in sorting should result in a change in the particle size distribution. Greater packing for cyclic shear loading, compared with monotonic (unidirectional) shear, may be explained by the relaxation of intragranular shear stress during the change from loading to unloading, thus allowing particles to re-position and fill voids. In both single- and multiple-cycle experiments the initial porosity reduction coincides with strain hardening, which is consistent with increased interlocking between particles as a result of lower porosity.

For  $\gamma \geq 0.8$ –1.0, both single- and multiple-cycle experiments exhibit dilatancy during slip and compaction upon unloading. Morrow *et al.* (1986) and Morrow & Byerlee (1989) report similar observations for experiments similar to our single-cycle experiments. In our experiments, dilatancy is not caused by decreased particle-size sorting in the bulk material, as this would appear as a change in the fractal dimension of the particle-size distribution, contrary to observation (Fig. 11). In addition, volume increase is not due to the formation of a fluid-pocket between the sample and jackets with offset, as indicated previously, and the porosity data are corrected for stress changes associated with sample offset. However, dilatancy and net volume increase with shear are consistent with unpacking of an overconsolidated material. Overconsolidation is used in soil mechanics to describe materials that are denser than the equilibrium porosity for a given state of stress (Lambe & Whitman 1968). In our experiments, shear-load cycles that result in negligible net slip cause overconsolidation, as indicated by net dilatancy in subsequent long-displacement cycles (Figs. 4a & b). Furthermore, the peak stress and form of the stress-strain

curves for multiple-cycle experiments are identical to those of overconsolidated soils (Lambe & Whitman 1968). Overconsolidation is also observed in connection with monotonic shear (Roscoe *et al.* 1958), which explains dilatancy in our single-cycle experiments. Roscoe *et al.* (1958) showed that for a wide range of initial densities, materials compacted prior to dilating during shear. Our results suggest that at 100 MPa, the gouge compacts initially to a lower porosity than the equilibrium porosity. In contrast, at 20 MPa, overcompaction and dilatancy do not occur. These observations suggest that dilatancy during shear for  $\gamma \geq 0.8$  is due to unpacking of an overconsolidated gouge. After shear localizes, unpacking would be limited to a narrow zone around shear bands, which may explain the slow dilatancy rate after  $\gamma \approx 1.3$ . We note that since an individual oblique shear band can accommodate only limited displacement due to geometrical incompatibility at the boundaries,  $R_1$  shears must form and die-out continually during shear.

#### Particle-size distributions

The comminution model presented by Sammis *et al.* (1987) predicts that gouge will obey a fractal particle-size distribution with fractal dimension 2.58 at steady state. In their model, fracture probability depends on the relative size of nearest-neighbor particles.

Our data show that gouge sheared to  $\gamma \geq 1.5$  at 100 MPa exhibits a fractal particle-size distribution with  $D = 2.6 \pm 0.15$ , indicating a steady-state particle-size distribution after  $\gamma = 1.5$ , according to the Sammis *et al.* (1987) model. Our mechanical and porosity data show slip at a constant stress and a roughly constant porosity, respectively, for  $\gamma > 0.8$ – $0.9$  and therefore agree with a steady-state gouge for  $\gamma \geq 1.5$ . In addition, our data indicate that one of the principal comminution mechanisms during shear at 100 MPa is crushing of similar-size particles. Particles within hydrostatically loaded layers undergo spalling and fracture along their edges, and significantly less overall comminution than sheared layers. This suggests that comminution is driven by relative movement between particles.

The fact that  $D$  levels-off at about  $\gamma = 1.5$  could result from either: (1) the particle-size distribution reaching a steady-state; or (2) a transfer of strain from the bulk material to shear bands. That is, if comminution is the result of shear displacement between particles, it may cease or decrease in rate within the bulk material once slip is localized.

Oblique,  $R_1$ , shear bands and boundary shears are first observed in our gouge layers at shear strains of 1.3–1.5. Both laboratory and field observations indicate that strain is concentrated along such features once they are formed (e.g. Mandl *et al.* 1977). In our experiments the shear bands consistently contain fewer large particles and have a smaller mean grain size compared with the bulk material. Thus, the fact that  $D$  for the bulk material levels off at about  $\gamma = 1.5$  is consistent with a transfer of slip from within the bulk material to shear bands, and

further supports the idea that fracture and comminution are driven by shear displacement between particles.

In the Sammis *et al.* (1987) model, fracture probability is greatest for particles with similar-size neighbors. Thus at steady-state, particles of similar size should not be nearest neighbors. However, unless large particles are continually added to the gouge zone during shear, the mean particle size must decrease with displacement; i.e. with sufficient displacement large particles will eventually come into contact and fracture. A decrease in mean size may occur without changing the relative proportion of particles within each size range, in which case the  $y$ -intercept in a plot such as Fig. 12 would decrease, but  $D$  would not change, or larger particles may be lost preferentially, in which case  $D$  would increase. The Sammis *et al.* (1987) model predicts the former case. Large particles should fracture and produce smaller particles, which should in turn fracture, keeping the relative proportion within each size range constant. Our data (Fig. 12) indicate that larger particles (25–50  $\mu\text{m}$ ) are lost preferentially within  $R_1$  shear bands. Thus, the breakdown of the fractal particle-size distribution for the shear bands results from a decrease in the upper fractal limit. This is consistent with small particles having a greater fracture strength than large particles. Thus, the smaller particles analyzed within shear bands ( $\approx 10 \mu\text{m}$ ) may represent a lower bound on the size-independent strength required by the Sammis *et al.* (1987) comminution model.

#### Shear localization

Since the early work of Reynolds (1885) and Mead (1925), shear localization within aggregate materials has been associated with dilatancy (e.g. Frank 1965, Mandl *et al.* 1977, Vardoulakis 1980). Mead (1925) pointed out that sands undergo either pervasive or localized deformation depending upon whether dilatancy is allowed or inhibited, respectively. Furthermore, he indicated that failure occurs via the mode that requires a minimum volume increase for a given displacement since this represents a minimum expenditure of work. Thus, according to Mead, strain should be pervasive if  $d\phi/d\gamma^B < d\phi/d\gamma^{SB}$  (where  $d\phi/d\gamma$  is the dilatancy rate and the superscripts refer to the bulk material and shear bands, respectively) and localized when the reverse is true. Frank (1965) continued this line of thinking, arguing that shear localization should occur within a deforming aggregate when  $d^2\phi/d\gamma^2$  changes from positive to negative. Frank's argument is that when  $d^2\phi/d\gamma^2$  is positive a given region cannot accommodate more strain than another region since, after an increment of strain with positive  $d^2\phi/d\gamma^2$ , the next increment of strain is most easily accommodated in a region with lesser strain due to its smaller volume increase with strain; i.e.  $d\phi/d\gamma$  is lower in regions with lesser strain when  $d^2\phi/d\gamma^2 > 0$ . Once  $d^2\phi/d\gamma^2$  becomes negative for a deforming aggregate the situation reverses, since the work done upon expansion in a given region decreases with each increment of strain. This provides the essential positive-

feedback needed to drive shear localization, since with each increment of strain  $d\phi/d\gamma$  becomes smaller and the work due to volumetric expansion decreases.

The data from our experiments agree with these general principles. Shear localization is not observed during the stage of overall compaction from  $\gamma = 0$  to 0.8. Instead, shear strain is pervasive in the gouge layers for  $\gamma \leq 1.3$  as indicated by microstructural observations and changes in the particle-size distribution of the bulk material. Dilatancy begins at about  $\gamma = 0.8$  in the single-cycle experiments, and the dilatancy rate during loading of a given cycle reaches a maximum at about this strain in the multiple-cycle experiments. Our porosity measurements are for the bulk material and thus the changes in  $d\phi/d\gamma$  that occur with load cycling are consistent with increasing  $d\phi/d\gamma^B$  from  $\gamma = 0$  to 0.8 and  $d\phi/d\gamma^B > d\phi/d\gamma^{SB}$  thereafter. The idea is that after  $\gamma = 0.8$  the dilatancy rate during loading is controlled by dilatancy within a localized zone, which does not change or changes slowly with strain. In addition, our porosity-strain curves begin to show a distinct inflection in second derivative at  $\gamma = 0.8$ –0.9. In multiple-cycle experiments the inflection occurs at about the peak stress for individual cycles, whereas in single-cycle experiments it occurs during slip. These observations suggest a transition from pervasive to localized strain at  $\gamma = 0.8$ –0.9. Although the first shear-localization features appear at  $\gamma = 1.3$ , localization could have begun prior to this, since this marks the onset of fully-developed shear bands.

The fact that shear bands first appear at about the same strain in single- and multiple- cycle experiments indicates that density alone does not control their formation. If this were the case shear bands should have appeared sooner in multiple-cycle experiments since porosity was significantly lower than in single-cycle experiments. Instead, the similarities in particle-size distribution and shear band development indicate a transition from pervasive to localized shear at a critical strain or particle-size distribution, in addition to the influence of density.

## CONCLUSIONS

Single- and multiple-load-cycle experiments exhibit different frictional behavior and porosity changes during shear. Compaction is observed together with strain hardening during the initial increments of shear strain in both cases. However, multiple-cycle experiments compact more rapidly and reach lower porosity than single-cycle experiments deformed to similar strains. In contrast, the particle-size distribution and microstructures are similar for the two types of experiments. In each case Riedel shears are observed after a shear strain of 1.3–1.5 at 100 MPa. The particle-size distribution obeys a fractal distribution for both single- and multiple-cycle experiments. The fractal dimension,  $D$ , of the distributions increases from  $1.8 \pm 0.15$  at 100 MPa and  $\gamma = 0$  to  $2.6 \pm 0.15$  after a shear strain of about 1.5.  $D$  remains  $2.6 \pm 0.15$  for  $\gamma = 1.5$ –3.3. On the basis of the difference in porosity and similarities in particle-size distribution we

conclude that initial porosity reduction and strain hardening in single-cycle experiments are due to changes in particle sorting and that additional compaction in multiple-cycle experiments is due to increased packing. The comminution rate of the gouge layer decreases at about  $\gamma = 1.5$ , which coincides with shear localization, suggesting that comminution occurs as a result of relative movement between particles. A comparison of the particle-size distribution for shear bands and the bulk material shows fewer large particles ( $>25$ – $50 \mu\text{m}$ ) within shear bands, indicating relatively large strains within the shear bands.

*Acknowledgements*—We thank Barry Raleigh and Fred Chester for helpful discussions and thoughtful reviews of the manuscript. Technical assistance by Ted Koczynski is gratefully acknowledged as is SEM work by Dee Breger. Dave Walker is thanked for helpful discussions in the early stages of this work. Lamont-Doherty Geological Observatory contribution No. 4492.

## REFERENCES

- Anderson, J. L., Osborne, R. H. & Palmer, D. F. 1980. Petrogenesis of cataclastic rock within the San Andreas fault zone of southern California. *Tectonophysics* **67**, 221–249.
- Anderson, J. L., Osborne, R. H. & Palmer, D. F. 1983. Cataclastic rock of the San Gabriel fault—An expression of deformation at deeper crustal levels in the San Andreas fault zone. *Tectonophysics* **98**, 209–251.
- Biegel, R. L., Sammis, C. G. & Dieterich, J. H. 1989. The frictional properties of a simulated gouge with a fractal particle distribution. *J. Struct. Geol.* **11**, 827–846.
- Blenkinsop, R. G. & Rutter, E. H. 1986. Cataclastic deformation of quartzite in the Moine thrust zone. *J. Struct. Geol.* **8**, 669–681.
- Byerlee, J. D. 1967. Frictional characteristics of granite under high confining pressure. *J. geophys. Res.* **72**, 36–39.
- Byerlee, J., Mjachkin, V., Summers, R. & Voevoda, O. 1978. Structures developed in fault gouge during stable sliding and stick-slip. *Tectonophysics* **44**, 161–171.
- Byerlee, J. & Summers, R. 1976. A note on the effect of fault gouge thickness on fault stability. *Int. J. Rock Mech. & Mining Sci. Geomech. Abs.* **13**, 35–36.
- Chester, F. M. 1988. The brittle–ductile transition in a deformation-mechanism map for halite. *Tectonophysics* **154**, 125–136.
- Chester, F. M. & Logan, J. M. 1987. Composite planar fabric of gouge from the Punchbowl fault, California. *J. Struct. Geol.* **9**, 621–634.
- Dieterich, J. H. 1981. Constitutive properties of faults with simulated gouge. In: *Mechanical Behavior of Crustal Rocks* (edited by Carter, N. L., Friedman, M., Logan, J. M. & Stearns, D. W.). *Am. Geophys. Un. Geophys. Monogr.* **24**, 103–120.
- Engelder, J. T. 1974. Cataclasis and the generation of fault gouge. *Bull. geol. Soc. Am.* **85**, 1515–1522.
- Engelder, J. T., Logan, J. M. & Handin, J. 1975. The sliding characteristics of sandstone on quartz fault-gouge. *Pure & Appl. Geophys.* **113**, 69.
- Epstein, B. 1947. The mathematical description of certain breakage mechanisms leading to the logarithmico-normal distribution. *J. Franklin Inst.* **244**, 471–477.
- Frank, F. C. 1965. On dilatancy in relation to seismic sources. *Rev. Geophys.* **3**, 485–503.
- Krumbein, W. C. & Sloss, L. L. 1951. *Stratigraphy and Sedimentation*. Freeman, San Francisco.
- Lambe, T. W. & Whitman, R. V. 1968. *Soil Mechanics*. John Wiley and Sons, New York.
- Logan, J. M., Friedman, M., Higgs, N., Dengo, C. & Shimamoto, T. 1979. Experimental studies of simulated gouge and their application to studies of natural fault zones. In: *Analysis of Actual Fault Zones in Bedrock*. *U.S. geol. Surv. Open-file Rept* **79-1239**, 276–304.
- Mandelbrot, B. B. 1982. *The Fractal Geometry Of Nature*. Freeman, San Francisco.
- Mandl, G., de Jong, L. N. J. & Maltha, A. 1977. Shear zones in granular material: an experimental study of their structure and mechanical genesis. *Rock Mech.* **9**, 95–144.

- Marone, C. 1989. Experimental studies of simulated fault gouge: frictional behavior, microstructures, and stability of sliding. Unpublished Ph.D. thesis, Columbia University.
- Marone, C. & Scholz, C. H. 1988. The depth of seismic faulting and the upper transition from stable to unstable slip regimes. *Geophys. Res. Lett.* **15**, 621–624.
- Marone, C., Raleigh, C. B. & Scholz, C. H. In review. Frictional behavior and constitutive modeling of simulated fault gouge. *J. geophys. Res.*
- Mead, W. J. 1925. The geologic role of dilatancy. *J. Geol.* **33**, 685–698.
- Moore, D. E., Summers, R. & Byerlee, J. D. 1988. Relationship between textures and sliding motion of experimentally deformed fault gouge: application to fault zone behavior. In: *Key Questions In Rock Mechanics* (edited by Cundall, P. A., Sterling, R. L. & Starfield, A. M.). *Proc. 29th U.S. Symposium on Rock Mech.*, Balkema, Rotterdam, 103–110.
- Morrow, C. & Byerlee, J. D. 1989. Experimental studies of compaction and dilatancy during frictional sliding on faults containing gouge. *J. Struct. Geol.* **11**, 815–825.
- Morrow, C. A., Lockner, D. & Byerlee, J. D. 1986. Velocity- and time-dependent stress transients in simulated fault gouge. *Proceedings of the International Symposium on Engineering in Complex Rock Formations*, Beijing, China, 142–148.
- Muhlhaus, H. B. & Vardoulakis, I. 1987. The thickness of shear bands in granular materials. *Géotechnique* **37**, 271–283.
- Olgaard, D. L. & Brace, W. F. 1983. The microstructure of gouge from a mining-induced seismic shear zone. *Int. J. Rock Mech. & Mining. Sci. Geomech. Abs.* **20**, 11–19.
- Petch, N. J. 1953. The cleavage strength of polycrystals. *J. Iron Steel Inst.* **174**, 25–28.
- Reynolds, O. 1885. On the dilatancy of media composed of rigid particles in contact. *Phil. Mag.* **S.5 20**, 469–481.
- Rogers, J. J. W. & Head, W. B. 1961. Relationships between porosity, median size, and sorting coefficients of synthetic sands. *J. sedim. Petrol.* **31**, 467–470.
- Roscoe, L. H., Schofield, A. N. & Wroth, C. P. 1958. On the yielding of soils. *Géotechnique* **8**, 22–53.
- Sammis, C. G. & Osborne, R. H. 1982. Textural and petrographic modal analysis of gouge from a depth of 165 m in the San Andreas fault zone. *Eos* **68**, 1109.
- Sammis, C. G., King, G. & Biegel, R. 1987. The kinematics of gouge deformation. *Pure & Appl. Geophys.* **125**, 777–812.
- Sammis, C. G., Osborne, R. H., Anderson, J. L., Banerdt, M. & White, P. 1986. Self-similar cataclasis in the formation of fault gouge. *Pure and Appl. Geophys.* **124**, 53–78.
- Scholz, C. H., Molnar, P. & Johnson, T. 1972. Detailed studies of frictional sliding of granite and implications for the earthquake mechanism. *J. geophys. Res.* **77**, 6392–6400.
- Shimamoto, T. & Logan, J. M. 1981. Effects of simulated fault gouge on the sliding behavior of Tennessee sandstone: nonclay gouges. *J. geophys. Res.* **86**, 2902–2914.
- Tchalenko, J. S. 1970. Similarities between shear zones of different magnitudes. *Bull. geol. Soc. Am.* **81**, 1625–1640.
- Underwood, E. E. 1968. Particle-size distribution. In: *Quantitative Microscopy* (edited by DeHoff, R. T. & Rhines, F. N.). McGraw-Hill, New York, 151–201.
- Vardoulakis, I. 1980. Shear band inclination and shear modulus of sand in biaxial tests. *Int. J. Numer. Analyt. Meth. Geomech.* **4**, 103–119.
- Wilson, E. B. Jr. 1952. *An Introduction to Scientific Research*. McGraw-Hill, New York.
- Yoshioka, N. 1986. Fracture energy and the variation of gouge and surface roughness during frictional sliding of rocks. *J. Phys. Earth* **34**, 335–355.
- Youd, T. L. 1972. Compaction of sands by repeated shear straining. *J. Soil Mech. Fdns Div. Am. Soc. Civ. Engrs* **98**, 709–725.